This article has been accepted for inclusion in a future issue of this journal. Content is final as presented, with the exception of pagination.

Dynamics of a High-Power AMB–Multirotor Drivetrain

Rafal P. Jastrzebski, *Senior Member, IEEE*, Atte Putkonen, Andrei Zhuravlev, Tuhin Choudhury, Eerik Sikanen, Emil Kurvinen, and Juha Pyrhönen, *Senior Member, IEEE*

(Post Conference Paper)

***Abstract*—Active magnetic bearings are commonly applied in high-speed rotors in the medium to high power range to replace rolling-element or oil-film bearings. They require less maintenance and provide a number of unique benefits owing to their contactless suspension and active control. A rotor construction with integrated compressors or turbines results in predictable and controllable rotor dynamics, where model-based controllers can be used. Model-based centralized controllers outperform decoupled transfer function controllers, but they require accurate plant models. For integrated impellers on a single rotor, the control models comprise a rigid rotor and the lowest frequency bending modes. The bending mode frequency and parameters related to node locations can be identified, yielding controllers tuned to the application. This work introduces drivetrain modeling and magnetic levitation control of a 2 MW rotor and an external load attached to the electric machine rotor with a radially stiff but flexural coupling. The model-based control is tested in an experimental setup, and the drivetrain frequency responses are compared with the modeled multirotor drivetrain dynamics.**

***Index Terms*—Finite element analysis, flexible structure, heat pumps, high-speed, induction motor, magnetic bearings, magnetic levitation, system dynamics, variable speed drives.**

Manuscript received 2 March 2023; revised 31 May 2023 and 31 July 2023; accepted 25 August 2023. This work was supported in part by the Academy of Finland under Grant 350880 and in part by the CoE Grant 346439. *(Corresponding author: Rafal P. Jastrzebski.)*

Rafal P. Jastrzebski is with the Department of Mechanical and Materials Engineering, University of Turku, 20014 Turku, Finland, and also with the Department of Electrical Engineering, Lappeenranta–Lahti University of Technology, 53850 Lappeenranta, Finland (e-mail: rafal.jastrzebski@utu.fi).

Atte Putkonen, Andrei Zhuravlev, and Juha Pyrhönen are with the Department of Electrical Engineering, Lappeenranta–Lahti University of Technology, 53850 Lappeenranta, Finland (e-mail: atte.putkonen@lut.fi; andrei.zhuravlev@lut.fi; juha.pyrhonen@lut.fi).

Tuhin Choudhury and Eerik Sikanen are with the Department of Mechanical Engineering, Lappeenranta–Lahti University of Technology, 53850 Lappeenranta, Finland (e-mail: tuhin.choudhury@lut.fi; eerik.sikanen@lut.fi).

Emil Kurvinen is with Materials and Mechanical Engineering Research Unit, University of Oulu, 90570 Oulu, Finland (e-mail: velimatti.kurvinen@oulu.fi).

Color versions of one or more figures in this article are available at https://doi.org/10.1109/TIE.2023.3317865.

Digital Object Identifier 10.1109/TIE.2023.3317865

I. Introduction

HIGH-SPEED and high-power electric machines are a promising technology that seeks to provide efficient and compact solutions for industrial application use, such as compressor, blower, chiller, and heat pump applications [1], [2], [3], [4]. For high-speed rotors in the medium to high power range, the industry has traditionally used rolling-element or oil-film bearings. Looking for a lower maintenance, oil-free, and more reliable replacement, various magnetic bearing solutions have been considered. Examples include repulsive permanent magnet bearings, [5] electrodynamic passive bearings [6], active radial dampers [7], various bearingless motors [8], and many variations of active magnetic bearings (AMBs) [9], [10]. AMB technology, in particular, has gained the most interest and could be considered well-established in the industry in those applications. It enables levitating the rotating part with low energy losses over a wide speed range and provides an opportunity to monitor and actively influence the behavior with a high sampling frequency. The high-performance active control of the AMBs is typically digitally implemented and model-based, i.e., there is a dynamical model available already in the system design phase. Currently, this is also being exploited and has further potential with the physics-based digital twins, where a virtual counterpart is used throughout the lifetime of the product and supports its operation [11].

Examples of the application potential are condition monitoring and maintenance, as they form the basis for system identification [12] and enable a comparison of the system behavior with respect to the model built. For fault identification purposes, a virtual counterpart can be used to study the parameter sensitivity and then gain an understanding of the individual product and use the generated data, e.g., for neural networks [13].

In addition to their main function as maintenance-free bearings, AMBs can be used to actively control vibrations, including, e.g., analysis and development of vibration modeling [14], suppression and investigation of vibrations, [15], [16], compensation of a runout [17], and unbalance [18].

Kumar and Tiwari [19] showed the identification of a system with two radial bearings to support the rotor. In [20], for the misalignment identification, a trial misalignment approach was proposed. Srinivas et al. [10] used an auxiliary AMB for fault identification and analysis of dual-coupled Jeffcott rotors

This work is licensed under a Creative Commons Attribution 4.0 License. For more information, see http://creativecommons.org/licenses/by/4.0/

This article has been accepted for inclusion in a future issue of this journal. Content is final as presented, with the exception of pagination.

supported by rolling-element bearings. The controllability of a flexible rotor against various unbalances was advanced by Noshadi and Zolfagharian [21], e.g., for unbalance and harmonic disturbance attenuation of a flexible rotor.

AMBs have been applied in high-speed rotating machines for decades, especially in integrated applications, such as compressors [22]. The scalability of integrated solutions is very limited because of the operation is close to the physical limits compromising dynamical behavior, mechanical rigidity, and thermal load [23], [24] to which, e.g., changes in geometry are significantly interconnected. Thus, the upscaling or application adjustments of these types of machines require extensive design iterations where all the factors have to be taken into account simultaneously. To design these machines, multidisciplinary convoluted approaches have been suggested, e.g., in [24]. We propose the deployment of a flexural coupling to allow the use of an AMB–rotor with different applications. It can be tailored based on application needs, and in the article, the feasibility of such systems is studied. The coupling affects the system dynamics, and thereby its controllability and performance. A case study of a multimegawatt (MMW) AMB–rotor described in [9] and [25] is used to analyze and verify the performance of the model-based control system. By this approach, the full machine redesign can be avoided in an integrated solution, such as a compressor or turbine application. A modeling approach to build a driveline model-based controller is also studied.

This work describes detailed modeling and experimental identification of coupled multirotor systems on AMBs for the very first time. In our case, the solid induction rotor has three radial AMB planes and six active-controlled DOFs, making it a particularly noteworthy industrial-size special case. In the literature, however, the multirotor dynamics of any AMB rotor system (being a standard or a special configuration) have not been discussed before.

Active vibration control of the drivetrain was considered in [26], but the drivetrain was not fully levitated, and ball bearings were used to reduce tangential friction and prevent a friction-driven response. The driveline misalignment leads to periodic parametric and forced actions that significantly affect the stability of the driveline and its vibration levels. To guarantee the closed-loop stability and adequate functioning of any driveline controlled by AMBs and subject to misalignment, it is essential to consider these effects when designing the control system. DeSmidt et al. [27] introduced a hybrid proportional derivative feedback coupled with a multiharmonic adaptive vibration control, specifically tailored for an AMB/U-joint-driveline system. The authors proved the convergence and robustness of the proposed approach, however, the machine is not considered to be a high-speed high-power one (the operating speed is 4815 r/min, and the torque load is 10 N · m, yielding a power of 5 kW). An adaptive notch filter was proposed in [28] for the driveline on AMBs, but the modeling of the whole driveline was not considered, and a PID controller was used for suspension.

The results presented by the authors in [1] are completely reworked, and new measurement and simulation results are provided. The control design and operation of a coupled AMB system are tested with speeds up to 7000 r/min, whereas previously, they have been tested only up to 4000 r/min in [1]. In addition radial, axial, and cross-coupling rotor dynamic frequency responses as well as loop sensitivity measurements of selected machine variants are presented and discussed. The drivetrain dynamics derived by the finite element method (FEM) are analyzed in addition to separate rotors.

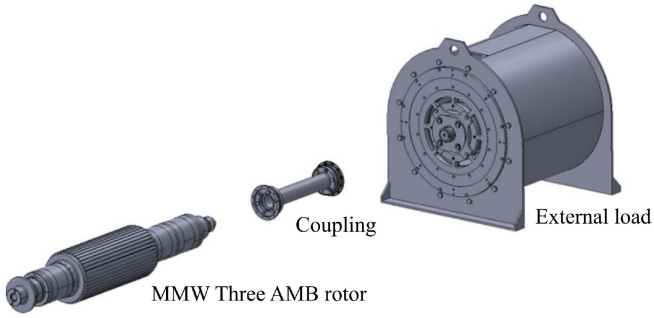

Fig. 1. Overview of the drivetrain comprising the MMW solid slit rotor with AMBs connected by a RENK coupling to the external load (Rotatek).

We propose a control methodology for a case where a radially rigid flexural coupling is used to connect the motor to the application, and a change in the dynamics is handled with the control of the AMBs. The analyses and experiments show that the dominant radial bending mode frequencies will be reduced, whereas the modal damping factors will increase. In parallel to control model identification, also an engineering nonlinear validation model that is an exact copy of the drivetrain is introduced.

II. Modeling of a Coupled Drivetrain

The controller uses a linearized coupled version of the plant model, which includes the MMW rotor with an added point mass representing the left-end flange of the coupling (see Fig. 1), linearized AMB stiffnesses, and simplified current-to-force dynamics. The initial controller employs the outermost radial AMBs and one axial AMB, resulting in a centralized four-degree-of-freedom (4-DOF) radial controller and a decoupled 1-DOF axial controller.

To verify the system behavior in the time domain, a nonlinear simulation plant model is built. The verification model incorporates a mechanical model of the entire drivetrain, which is dependent on the system speed, nonlinear actuators, and discrete cascade controllers. The nonlinear actuator models use stiffness and inductance values (which depend on currents and air gaps) represented as look-up tables (LUTs), which are computed based on electromagnetic FEM models. The mechanical models derived by using the FEM use modal reduction for computational efficiency.

A. Mechanical Rotor Models

To obtain the equation of motion, finite-element analysis is employed, which involves discretizing the rotor shaft into 3-D beam elements based on Timoshenko's beam theory [29].

This article has been accepted for inclusion in a future issue of this journal. Content is final as presented, with the exception of pagination.

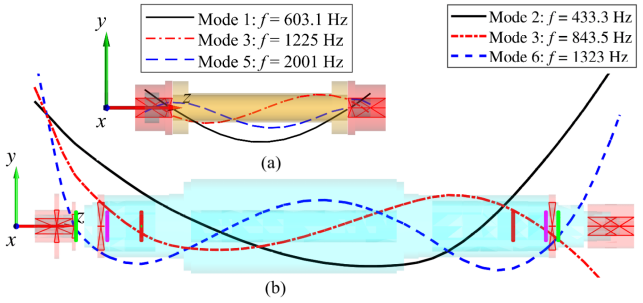

Fig. 2. Retained free–free mode shapes and their respective frequencies for (a) coupling including closed flanges on both ends and (b) MMW rotor (bearing, sensor, and retainer bearing nodes are indicated by purple and green lines) with an added point mass at the drive end corresponding to the coupling flange (motor and coupling tube halves together).

We constrain the mechanical FEM to xy in-plane DOFs. Every node on the rotor has four DOFs, where two are for translation and the other two for rotation. This simplifies the model by neglecting motion in the z-direction. For AMB–rotor systems, 4-DOF models are sufficient for control plant and verification plant modeling, where out-of-plane motion is less critical. We show by experimental data (in Section IV) that, in fact, there is a coupling in the drivetrain dynamics between the xy plane and the z direction. However, it is attributed to frame components not modeled in the study.

To simplify the model, radial AMB laminations can be treated as mass points and added to their corresponding nodal locations. Alternatively, they can also be modeled as beams with a reduced stiffness, where the reduction in stiffness is tuned so that the responses of the rotor model correspond to the measured ones. By this approach, a sufficient level of accuracy can be achieved to effectively design a rotor and a controller for AMBs [9].

Fig. 2 illustrates the lowest frequency mode shapes and their corresponding frequencies for the MMW rotor and the coupling. The predicted natural frequencies and mode shapes are calculated for free–free boundary conditions. We experimented with two coupling models. The first one has the stiffnesses of the flexural disc pack elements embedded in the FEM element list, and it uses radial, axial, and rotational stiffnesses. This results in Fig. 2(a). The second one comprises only a coupling tube, and the localized stiffnesses of the disc packs are connected to the relative displacements of the end nodes as input forces. Only the radial stiffnesses are used as the reduced discrete element models have only radial displacement outputs and radial force inputs. This approach allows us to keep the same AMB rotor model in the controller as in the plant. Both approaches result in a similar final drivetrain model (virtual prototype).

In the FEM interface, the inputs for each rotor model in the drivetrain (MMW, RENK, and Rotatek) consist of geometrical dimensions and material properties of the rotor (see Fig. 3). The FE models of each component of the drivetrain are adjusted individually so that the free–free frequencies match the ones obtained by the experimental modal analysis. This standard method of verification ensures the dynamic accuracy of the individual rotor models.

For the active part of the MMW, 3-D beam elements are insufficient to accurately represent the complex slit rotor structure. As a result, the cross-sectional properties of the slitted area are calculated from the CAD model and incorporated into the FEM. To enhance accuracy, the sensors, spacers, laminations, and properties of the slitted section of the active part (such as elasticity and density) can be adjusted based on measured frequency responses.

For the RENK coupling, beam elements represent the flanges and the cylindrical hollow section. The flanges on each side are linked to the central hollow tube section by thin plates, which contribute to the overall flexibility of the coupling. These plates are modeled as springs, and their properties are adjusted to match the directional stiffness provided in the manufacturer's catalog. The external load machine from Rotatek (previously Yaskawa Environmental Energy) is also simplified in a similar way.

The number of nodes was selected to accurately model all the geometrical features of the rotors. Finally, the long uniform beams were also divided into smaller elements. The AMB–rotor was modeled precisely, whereas the load machine rotor was modeled less accurately. The base, frame, and all the other components, such as actuator stacks, will affect the final dynamical behavior of the plant as seen by the sensors of the AMB controller.

The dynamics of elastic rotors can be expressed as a combination of elastic and inertial forces acting on a beam. In the case of the Euler beam equation, the free bending vibrations that occur in the yz plane can be described by a partial differential equation along z in time t

$$EJ\frac{\partial^4 w}{\partial z^4} = q \tag{1}$$

where q, w, and EJ are the force per unit length, the deflection of the beam in the y direction, and the stiffness, respectively.

In a Timoshenko beam with a uniform cross-section, the force acting on the beam displacement w per unit length is reduced because of the shear force

$$EJ\frac{\partial^4 w}{\partial z^4} = q(z) - \frac{EJ}{\kappa A G_1}\frac{d^2 q}{dz^2} \tag{2}$$

with G_1 being the shear modulus. κ and A are the Timoshenko shear coefficient and the cross-sectional area, respectively.

By using the boundary conditions of the beam element attachments and the initial conditions for displacement and velocities, a solution is obtained. The solution comprises an infinite series of eigenfunctions described by the natural frequencies ω_i, where i ranges from one to infinity. The eigenvectors define unique mode shapes with arbitrary amplitudes. Following the modal reduction, the modal rotor dynamics comprises both the rigid body modes and the dominant bending rotor modes. The number of bending modes with the lowest natural frequencies are retained, and the time behavior of each natural vibration follows a second-order resonator. For instance, the first bending mode, represented by the banana-shaped mode of the MMW in Fig. 2(b), has the lowest natural frequency and is described as

$$m_1\ddot{y}_1 + d_1\dot{y}_1 + k_1 y_1 = 0 \tag{3}$$

This article has been accepted for inclusion in a future issue of this journal. Content is final as presented, with the exception of pagination.

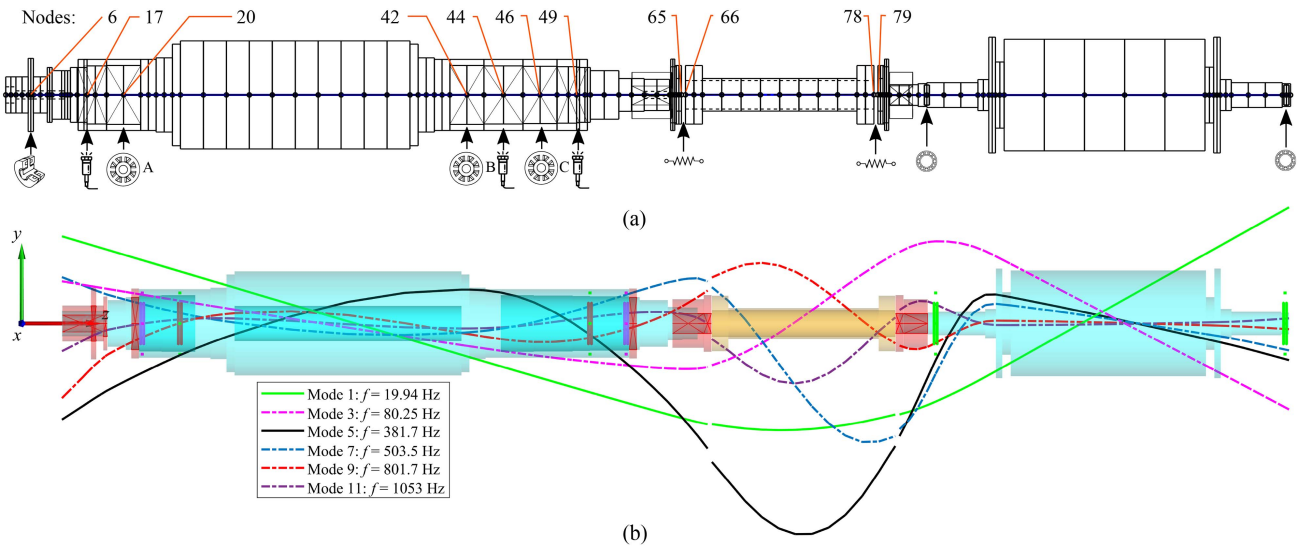

Fig. 3. (a) Drivetrain FEM model indicating the positions of various components, such as the axial AMB, sensors, radial AMBs, coupling springs, and ball bearings in the load machine. The MMW rotor alone has 65 nodes (including node 0) and 260 DOFs. Between the nodes, there are shaft beams, component tubes (up to three layers with the shaft), and point mass elements for lock nuts and flanges. (b) Full drivetrain model with the shape of the modes and the corresponding frequencies.

$$d_1 = 2\zeta_1\omega_1 m_1, k_1 = \omega_1^2 m_1 \tag{4}$$

where ζ_1 is the relative damping. m_1, d_1, and k_1 are the modal mass, the absolute damping, and the modal stiffness, respectively.

By setting state variables equivalent to the displacement vector, which includes rigid rotor modal displacements in the center of gravity (COG) coordinates and modal displacements, as well as velocities, the control plant can be represented in the state variable form. The control current vector acts as the input, and the rotor displacement vector at the sensor locations is the output

$$\boldsymbol{\eta} = \begin{bmatrix}\mathbf{x} & \dot{\mathbf{x}}\end{bmatrix} \tag{5}$$

$$\dot{\boldsymbol{\eta}} = \mathbf{A}_\mathrm{r}\boldsymbol{\eta} + \mathbf{B}_\mathrm{r}\mathbf{u}, \mathbf{y} = \mathbf{C}_\mathrm{r}\boldsymbol{\eta} \tag{6}$$

$$\mathbf{A}_\mathrm{r} = \begin{bmatrix} \mathbf{0} & \mathbf{1} \\ -{\mathbf{M}_\mathrm{m}}^{-1}\left(\mathbf{K}_\mathrm{m} - \mathbf{T}_\mathrm{a}^\mathrm{T}\mathbf{K}_x\mathbf{T}_\mathrm{a}\right) & -{\mathbf{M}_\mathrm{m}}^{-1}\left(\mathbf{D}_\mathrm{m} + \Omega\mathbf{G}_\mathrm{m}\right) \end{bmatrix}$$

$$\mathbf{B}_\mathrm{r} = \begin{bmatrix}\mathbf{0} & {\mathbf{M}_\mathrm{m}}^{-1}\mathbf{T}_\mathrm{a}^\mathrm{T}\mathbf{K}_i\end{bmatrix}^\mathrm{T}, \mathbf{C}_\mathrm{r} = \begin{bmatrix}\mathbf{T}_\mathrm{s} & \mathbf{0}\end{bmatrix}.$$

The locations of the sensor and actuator nodes are generally known. Relative damping can be estimated using the half-power method based on experimental frequency responses. The modal amplitudes are scaled by the modal mass. If the rotor is axisymmetric, the dynamics are the same in the xz and yz planes. The rotor mass, stiffness, damping matrices, and the state variable vector can be expressed in the COG modal coordinates as

$$\mathbf{M}_\mathrm{m} = \mathrm{diag}\left(m, m, I_x, I_y, m_1, m_1\right)$$

$$\mathbf{D}_\mathrm{m} = \mathrm{diag}\left(0, 0, 0, 0, d_1, d_1\right)$$

$$\mathbf{K}_\mathrm{m} = \mathrm{diag}\left(0, 0, 0, 0, k_1, k_1\right)$$

$$\mathbf{x} = \begin{bmatrix}x & y & \varphi_x & \varphi_y & x_1 & y_1\end{bmatrix}^\mathrm{T}.$$

The AMB stiffness matrices $\mathbf{K}_i$ and $\mathbf{K}_x$ are of a diagonal form. Ω is the rotational angular velocity.

In the plant model, forces and moments are introduced through the AMB locations, and rotor displacements are monitored at the sensor locations. The transformation matrices $\mathbf{T}_\mathrm{a}$ and $\mathbf{T}_\mathrm{s}$ convert the coordinates from the COG of the rotor into the sensor and actuator frames

$$\mathbf{x}_\mathrm{a} = \mathbf{T}_\mathrm{a}\mathbf{x}, \mathbf{x}_\mathrm{s} = \mathbf{T}_\mathrm{s}\mathbf{x}. \tag{7}$$

The forces and moments in the bearing frame follow the transformation into the COG of the rotor frame

$$\mathbf{F} = \mathbf{T}_\mathrm{a}^T\mathbf{F}_\mathrm{a}. \tag{8}$$

The model (6) is linear except for the case with the variable speed Ω.

B. AMB Models

The linearized control plant model combines the current and position stiffnesses of the bearing with the modal-reduced rotor in the state–space form (6). For example, the linearized forces along the control x-axis are

$$F_x = k_i i_{cx} + k_x x. \tag{9}$$

The current stiffness k_i and the position stiffness k_x are defined at the operating point ($x = 0$, $i_\mathrm{c} = 0$) with the assumptions of no saturation, no fringing flux paths, and force geometric decoupling in the analytical equations

$$k_i = \frac{\mu_0 N^2 S\cos\xi i_\mathrm{b}}{l_0^2}, k_x = \frac{\mu_0 N^2 S\cos\xi i_\mathrm{b}^2}{l_0^3} \tag{10}$$

where ξ is the geometric force acting angle, N is the number of turns, l_0 is the mean air gap, and μ_0 is the permeability of air.

This article has been accepted for inclusion in a future issue of this journal. Content is final as presented, with the exception of pagination.

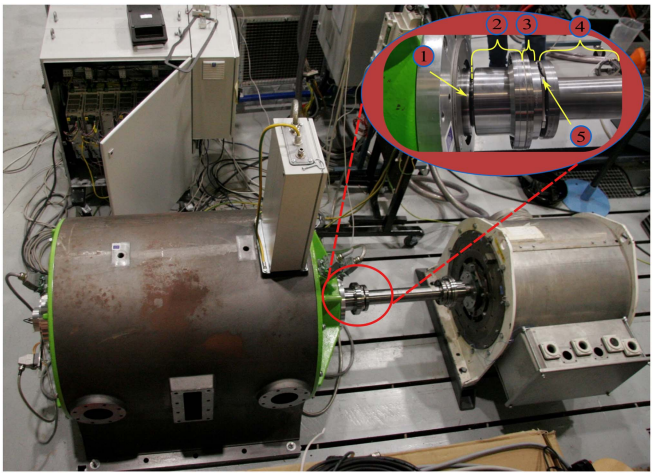

Fig. 4. Drivetrain with the control electronics and the inverter cabinets. The MMW has green bearing shields on the sides, and the Rotatek load is on the right-hand side. The zoomed area is the DTM RAFLEX133 flexible disk coupling connection to the MMW. 1—motor end, 2—motor coupling flange (motor half), 3—tube coupling flange (tube half), 4—coupling middle tube, and 5—flexural disc.

However, accurate values are taken from the electromagnetic FEM (JMAG) simulations or measured experimentally [9]. In addition, the inner current-controlled closed-loop dynamics can be identified from the measured frequency responses. Consequently, the inner-loop current dynamics are added in series to the rotor dynamics in the complete control model.

For control validation in MATLAB Simulink, nonlinear force, and inductance relations dependent on displacements and currents [1] are represented as LUTs. The force and voltage equations of the actuator model use interpolated parameters from those LUTs. Pulsewidth modulation and transportation delays, inner-loop discrete regulators, and signal limitations, i.e., the dc link voltage limit and the maximum available amplifier current limits, are also implemented.

C. Drivetrain Model

The MMW, RENK coupling, and Rotatek load machine rotors are represented using the FEM coded in MATLAB, generally based on [30]. To simplify the model, only a few bending modes are retained for each rotor after the modal reduction. In the case of the Rotatek load machine, rigid modes are not included, because it uses ball bearings, and the forces can only affect its bending. The equations describing the multirotor dynamics are assembled by overlapping the terminal node locations of all three parts, resulting in a state variable form as (6). The motor models connect through the coupling, where the coupling tube is modeled as 3-D beam elements, and each disc pack is represented by a localized directional stiffness (e.g., for the x direction, the tuned values are radial k_{xx} = 4.32e8 N/m and bending $k_{\phi_{xx}}$ = 6.54e6 N · m/rad) and damping (radial d_{xx} = 2.5e-5·k_{xx} and bending $d_{\phi_{xx}}$ = 2.5e-5·$k_{\phi_{xx}}$). The spring damper elements connect the middle tube of the RENK coupling to the coupling flanges fitted on the MMW (see the zoomed area in Fig. 4) and the Rotatek rotors. The axial stiffness of the coupling was provided in the datasheet, but the radial and bending stiffnesses were missing. To estimate these stiffnesses, first, in the CAD model, the modulus of elasticity is tuned using a linearized force displacement equation $F_{\mathrm{c}} = k_{\mathrm{ca}}x$ for the unit force F_{c} and the known localized axial coupling stiffness k_{ca} = 7.77e5 N/m. The mass of the coupling m_{c} is then used in the eigenvalue solution for the corresponding mode and natural frequency $k_{\mathrm{c}} = {\omega_{\mathrm{n}}}^2 m_{\mathrm{c}}$ to obtain the directional radial and bending stiffnesses [31]. The above tuned values are up to 20% larger than the ones obtained from the eigenvalue solution and tuned to the bending mode frequencies from the experimental modal analysis. The approach of modular modeling is advantageous as the control plant can use the same MMW model that is applied in the drivetrain. However, the dynamics of the drivetrain obtained from this method are prone to errors in model reduction and the number of dominant modes retained in each rotor.

An alternative modeling approach could be to consider the whole drivetrain as a single structure [see Fig. 3(b)], and then obtain the control plant model after the modal reduction. This would allow easy access to the free–free mode shapes of the connected drivetrain. However, this approach does not provide a direct way to obtain the control MMW plant from the drivetrain model, making the model reduction for control purposes a challenge. One solution to this could be to use manually generated rigid body modes of the MMW rotor while importing the first (or any needed control number) lowest bending mode shape to it from the drivetrain model.

III. Control

When a plant model is available, a number of model-based control techniques can be applied. One way is to use the H-inf or linear-quadratic-Gaussian (LQG) control at a certain speed. It makes sense to use linear parameter-varying or modal control if speed is a variable parameter. Present synchronous disturbances can efficiently be suppressed with different unbalance force rejection and synchronized displacement suppression methods. The main point of this article is to show that even a basic model-based control is a good enough solution when an accurate plant model is available.

The control plant that is used for control synthesis takes into account the rigid body modes and the first (dominant) lowest-frequency bending modes of the MMW, but for verification purposes, the plant with three bending modes is used in the simulation model. Zhuravlev et al. [32] pointed out that the control plant with the speed closer to zero rather than to the maximum is used for optimal performance with respect to external disturbances in the case of nonadaptive controllers.

In the case of three radial AMBs, the model-based LQG controller with the integral (per axis) can not withstand eccentricity in the location of the middle radial AMB. Therefore, some control strategy, such as the H-inf controller that does not have an integral has to be used. The general control block diagram is shown in Fig. 5.

This article has been accepted for inclusion in a future issue of this journal. Content is final as presented, with the exception of pagination.

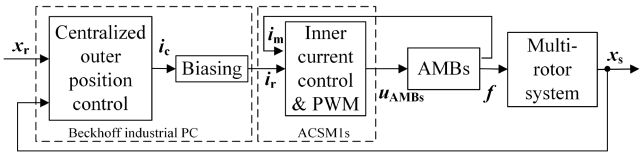

Fig. 5. General cascade control architecture applied in the study. The outer position controller is implemented in the Beckhoff power line carrier, whereas the inner current controllers are implemented in the field programmable gate arrays (FPGAs) interfacing with the AMB ACSM1s.

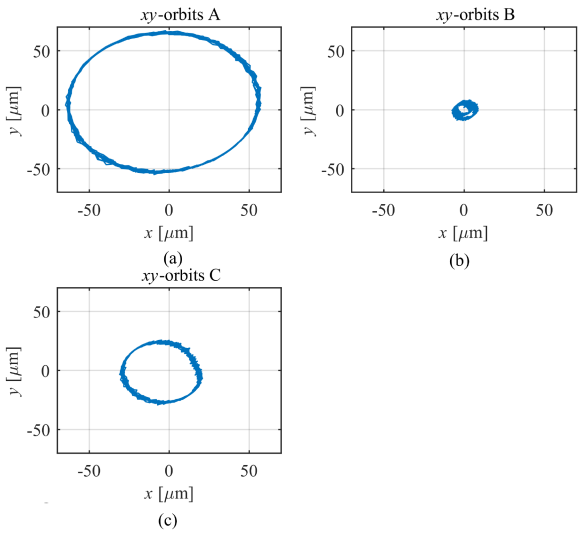

Fig. 6. Simulated orbits at 7000 r/min when the AMB–rotor is connected to an external load. (a) Sensor A. (b) Sensor B. (c) Sensor C.

A. Control Simulations

Cascade control consists of an outer position control loop with an LQG controller (synthesized at a fixed speed) and an inner current loop with a PID controller. The nonlinear drivetrain model (see Fig. 3) used for testing has several modes in each rotor, and the speed as the external input. The force and inductance LUT nonlinearities, signal saturation, noise, and delays are taken into account. The MMW model and the LQG control are adopted from [8], but the control plant model is updated according to the measured drivetrain dynamics. Fig. 6 shows position orbits from an exemplary nonlinear time simulation scenario. The signal noise levels in all channels are set to the maximum noise values measured from the experiment. The sensor runout is assumed to be 18 μm for the first harmonic and 5 μm for the second harmonic with the same phases in channels A and B and inverted phases in channel C. Small unbalance forces are added to the nodes corresponding to the center of the MMW rotor and to the coupling flange point masses.

IV. Experimental Results

A. Control Plant Tuning Based on Frequency Responses

First, the stand-alone MMW rotor is commissioned. The LQG optimal control uses weighting matrices where the initial tuning coefficients are generally based on signal noise covariances. For

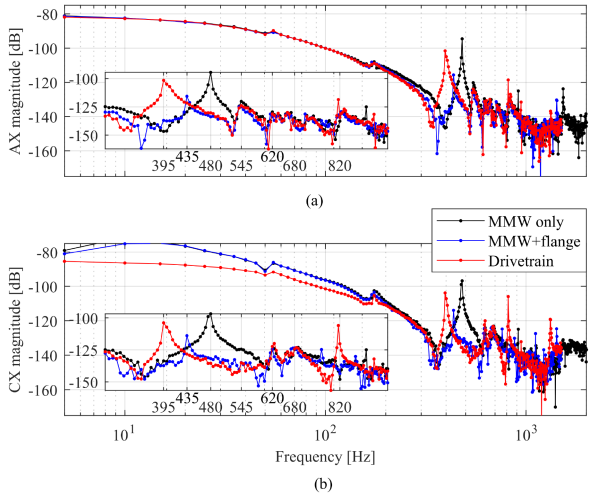

Fig. 7. Measured frequency response magnitudes of the MMW rotor (black), the MMW rotor with a coupling flange part (blue), and the assembled drivetrain (red), see Fig. 1. The gain from the excitation (0.2 A control current amplitude) to the rotor displacement in (m) is measured by (a) sensor A and (b) sensor C in the x-axis.

the measured radial and axial currents, the standard deviations are in the range of 0.279–0.433 A and 0.194–0.241 A, respectively. The ranges of 0.616–0.890 μm for the measured radial positions and 2.611 μm for the axial position are recorded. The frequency responses of the plant are captured with the initial controller (see Fig. 7, black). Here, the excitation is added to the control currents one input at a time. The identification results are used to tune the MMW rotor model. The following step is to include details of the rotor, i.e., an additional point mass of the coupling flange is added to the rotor end, and the plant model and the controllers are recomputed. The coupling has a mounting mechanism where the left half of the flange (the motor half) is fitted to the rotor, whereas the other half (the extension tube half) is connected through flexural elements to the coupling middle tube. During the installation and assembly, those two flange halves are rigidly connected. It is not possible to carry out identification of the stand-alone MMW rotor with the added point masses of both flange halves as the right flange half cannot be separated from the coupling tube. The stand-alone rotor with half of the flange is measured when the tube half and the subsequent elements are disassembled, as shown in Fig. 7 (blue). The rotors of the drivetrain illustrated in Fig. 4 are aligned, and the MMW rotor is levitated while connected through the coupling. At this point, the frequency responses can be captured for the connected drivetrain (see Fig. 7, red).

In the control plant model, only the rigid MMW rotor (with the coupling flange-added point mass) and the first bending mode are retained. This mechanical plant model is tuned so that its Bode magnitude frequency responses correspond to the experimentally measured ones but of the whole drivetrain. Such a simplification is possible because of the relatively low stiffness coupling and the high frequency of the other rotor bending modes.

The x- and y-planes are assumed identical in the modeling of the rotor dynamics. However, the experimental data give

This article has been accepted for inclusion in a future issue of this journal. Content is final as presented, with the exception of pagination.

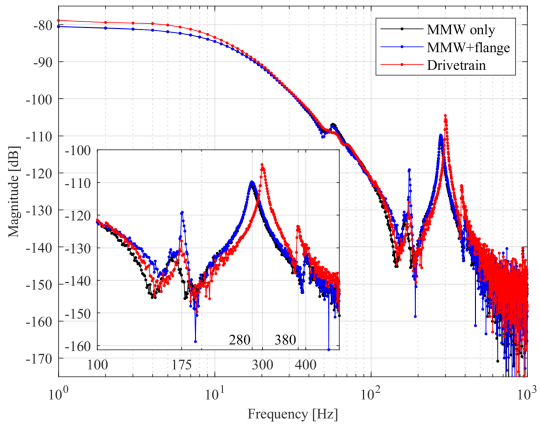

Fig. 8. Measured frequency response magnitudes in the axial direction of the MMW rotor (black), the MMW rotor with a coupling flange (blue), and the assembled drivetrain (red). The gain from the excitation (2 A control current amplitude) to the rotor displacement [in (m)] is measured in the z-axis.

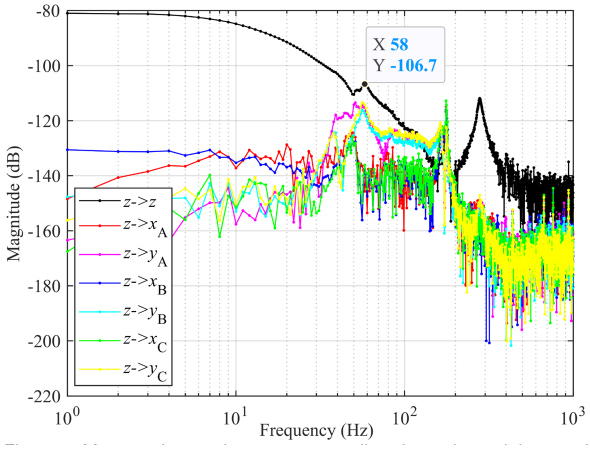

Fig. 9. Measured open-loop cross-coupling from the axial control current to the measured rotor displacements of the MMW rotor alone but with a coupling flange. The gain from the excitation (2 A control current amplitude) to the rotor displacement [in (m)] is measured in the xyz axes in the ABC sensor planes.

different responses. The reason for this is the nonaxisymmetric geometry of the motor housing and support, as well as the housing and support of the external load. Because of the decoupling effects, mainly the motor tubing and housing contribute to the plant dynamics. The gravity vector is oriented in the negative y-axis direction. The machine frame is bolted to the concrete test bench, and it is more rigid along the y-axes of all the AMBs.

A similar procedure is carried out for the tuning of the axial controller (again based on the measured frequency responses as in Fig. 8), which is assumed for the purposes of control tuning to be decoupled from the radial one. When examining the cross-coupled terms in Fig. 9, one can see that, in fact, the low-frequency mode at 58 Hz is strongly coupled with the y-axis and weaker with the x-axis radial dynamics, whereas the 175 Hz mode is coupled very strongly with the x-axis and weaker with

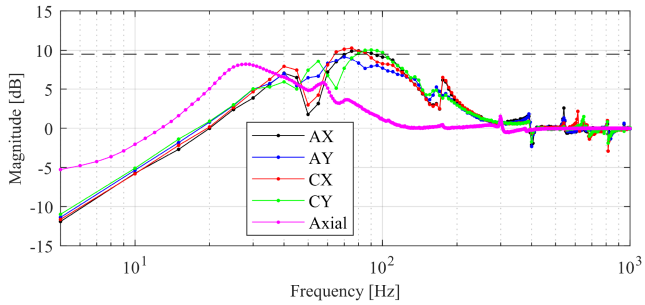

Fig. 10. Measured sensitivity function of the drivetrain in the radial and axial directions when the LQG controller is applied. The Zone A limit of 9.5 dB is indicated by a dashed line.

the y-axis radial dynamics. With the coupling assembled and connected, these two modes are damped and less visible in the axial dynamic responses but more visible in the radial dynamic responses. The frequency of the higher frequency mode (279 Hz) in the z direction increases when its damping decreases in the drivetrain connection. This is a reversed trend compared with the radial dynamics and the first bending mode at 480 Hz, which changes to 395 Hz in the drivetrain (see Figs. 3 and 7). The origin of axial resonance at 279–299 Hz is not known, but it does not couple with the radial dynamics. Moreover, its frequency is high enough and does not affect the axial controller. The two modes at 58 and 175 Hz that are visible in both the radial and axial dynamics can be included as uncertain, e.g., additive uncertainty and as a transfer function weight in the plant model. This enables the use of μ-synthesis for the controller design, and further, it acts as a notch filter and improves closed-loop responses at those frequencies. In addition, the weak resonance peaks of 620 and 680 Hz shown in Fig. 7 do not match with any modeled drivetrain bending mode frequencies.

The measured sensitivity peaks for the radial direction are in Zone B according to ISO 14839-3 but barely crossing the Zone A limit of 9.5 dB, as shown in Fig. 10. With tuning of the controller, Zone A is possible. The peak for the axial direction is below the limit.

B. Experimentation With the Rotating System

After the tuning of the controller when taking into account the changed dynamics of the first bending mode of the MMW rotor connected to the drivetrain, the rotors are rotated. Fig. 11 presents the measured orbits and positions of all the AMB sensors at 7000 r/min. Fig. 12 shows the maximum rotor center deviation during acceleration of the rotors.

V. Discussion

Typical commercial configurations in high-speed and high-power machines are integrated, i.e., the motor and the application are being combined. The oil bearings are replaced with magnetic bearings, and the gearbox is eliminated. This leads to a high-performing machine that has a small factory footprint. High-speed AMB–rotor systems are the state of the art for integrated compressors. However, because of the integrated

This article has been accepted for inclusion in a future issue of this journal. Content is final as presented, with the exception of pagination.

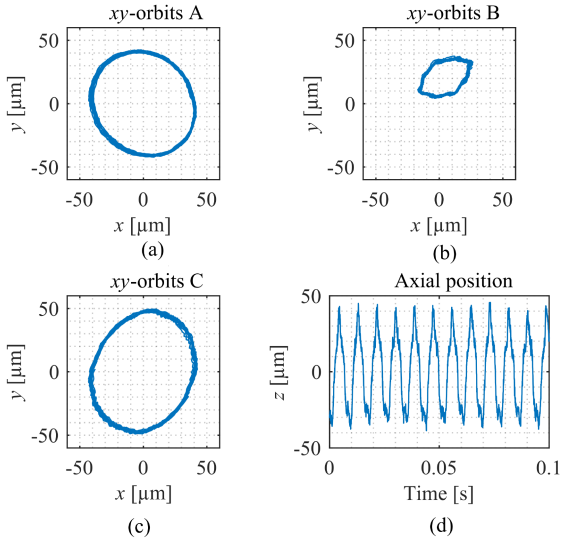

Fig. 11. Measured orbits at 7000 r/min when the AMB–rotor is connected to an external load. (a) Sensor A. (b) Sensor B. (c) Sensor C. (d) Axial position.

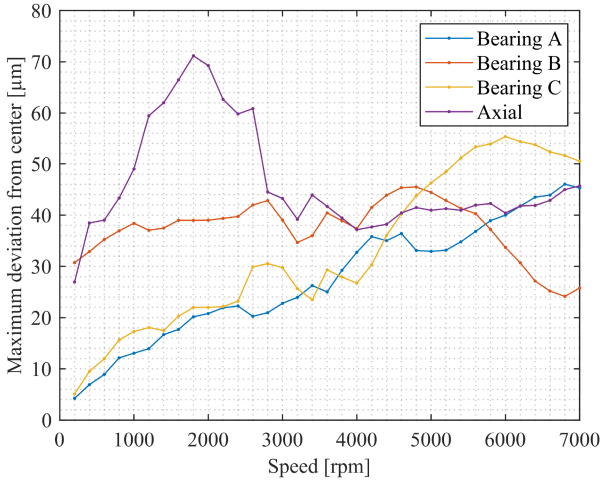

Fig. 12. Measured maximum rotor center deviation from the mean position of the rotor in the ABC radial sensor planes and in the axial direction during the run-up of the speed ramp.

solution, the scalability for higher speeds or powers requires large and timely design iterations, as the speed and size are limited by the dynamics and stresses. In addition, alternatives to AMBs, such as high-power bearingless technology, are still in the early commercialization stage for compressor applications, as reported, e.g., in [8] and [24]. To overcome the scalability issue, a flexural coupling is proposed. Decoupling between the MMW and the load is mostly achieved through flexibility that comes from the flexural coupling disc packs. The central tube length is a consequence of the application and coupling sizing, but the flexibility of the tube provides added decoupling. In general, lower coupling stiffness values decouple the high-frequency dynamics better. However, for some drivetrains and controllers, a very low stiffness of the coupling can compromise the stability margins at low frequencies. The detailed stability analysis as a function of the coupling stiffness of the closed-loop system is a complex problem, intertwining both the control and the plant.

The three-bearing solution brings additional capabilities compared with the two-bearing solution. Placing three radial actuators at one shaft brings a number of advantages, such as better opportunities for identification of the rotor dynamics, better visibility of the rotor bending modes by the controller, better controllability of the bending modes, a more robust control in the presence of changeable dynamics because of the application, a higher bandwidth of the actuators, and multiple unique coupled and decoupled control options (being outside the scope of this study). In addition, three actuator planes provide redundancy in safety and can be arranged in different control layouts. For example, two actuators on the drive-end side can be arranged as a single bearing configuration, or one bearing can be dedicated to active damping and external disturbance compensation, while the remaining two focus on the levitation. The three-bearing solution yields a marginally longer rotor with lower bending mode frequencies. However, the machine stays subcritical.

The modeling of the drivetrain was implemented by two different methods, in the first method, the connected rotors were modeled separately and the modal-reduced rotors were connected together, whereas in the second approach, the whole drivetrain was modeled as a whole. For the radial dynamics, the state matrix eigenfrequencies of the connected structure are lower compared with the eigenfrequencies of the MMW (AMB-controlled) rotor alone. This is confirmed by the experimental frequency responses.

The high peaks in the frequency responses correspond to the resonance frequencies of the system under study. The natural frequencies of the system are defined from the relationship of the material structural stiffness, i.e., the modulus of elasticity, and the mass. External resonances may also influence the system frequency response.

Two lower frequency resonances at 55 and 175 Hz can be observed in both the radial and axial dynamics, but they cannot be associated with the lower bending modes derived for the FEM model of the drivetrain [see Fig. 3(b)]. Those mode frequencies change slightly with the rotor configuration. The peak at 55 Hz relates to the frame longitudinal (lengthwise) vibration, which couples with the radial direction because of the frame and end shield twisting. The peak in the 150–175 Hz range is associated with the end shield torsional twisting with a very strong coupling between the radial and axial directions. The 175 Hz mode is mostly visible in the nongravity x-direction. The AMB–rotor and the external load housings are rigidly supported in the y-direction. Modifying the MMW rotor by adding the half-flange of the coupling or closing the coupling flange changes the dynamics of the rotor, whereas the frame dynamics as seen by the sensors of the AMB-controlled rotor remain unchanged. Adjusting the coupling allows a certain degree of manipulation of the resulting dynamics. For example, the flexible modes can be shifted to lower frequencies that can be passed at low speeds, and operation can commence in the speed range between flexible

This article has been accepted for inclusion in a future issue of this journal. Content is final as presented, with the exception of pagination.

modes. Changes in the coupling stiffness, especially loosening, will lower the resonance frequencies.

In the experimental modal analysis made for the MMW frame without other components, a peak of 667 Hz was observed. This frequency corresponds to the horizontal twisting mode of the frame. Additional components installed in the frame, such as a stator, can have a stiffening effect, and thus increase the frame twisting mode to reach 680 Hz, which can be seen in the measurements in Fig. 7. Because the electrical machine is equipped with AMBs, the modal coupling between the rotor and the frame is usually not significant. Still, any changes to the system can affect the resulting dynamics. As an illustration, adding a motor stator to the tubing increased the 620 Hz resonance peak in the radial responses compared with the system prior to the stator assembly.

With the tested speeds reaching 7000 r/min, the peak of the closed-loop sensitivity function remained below 12 dB, which corresponded to the acceptable performance class according to ISO 14839-3 [33].

We investigated the inclusion of a frame model together with the electromagnetic and rotor models. However, in our opinion, the significant complexity of the overall model when the nonsymmetric frame is added does not justify that kind of model extension.

VI. Conclusion

The study described and demonstrated high-speed driveline analysis and modeling methods with experimental verification.

We proposed a flexible coupling to connect an AMB-supported MMW rotor to another machine. The system was analyzed by creating rotordynamic models for the MMW, the coupling, and the load machine by using modal reduction and connecting the rotordynamic models together. An alternative formulation of the mechanical model was discussed. The obtained rotordynamic drivetrain model was connected to the three radial AMB nonlinear actuator models and the magnetic bearing control equations. The modeled dynamics and examples of simulation scenarios were compared with experiments. Measurement results were presented including radial and axial frequency response plots and displacement response data from 0 to 7000 r/min.

Changes in the dynamics were considered by retuning the control models from the frequency responses of the laboratory multirotor system. A control plant, including a single rigid rotor with the retained first bending mode with a changed frequency, resulted in good performance indices when measuring the output sensitivity according to the ISO 14839-3 standard.

For the control model, the electric machine rotor, the coupling, and the load machine could be modeled separately. The modal-reduced individual rotors could be assembled into a verification model, which could be used in the control design and simulations. The rotors were connected through forces acting on both sides of the coupling, as they were in the physical systems. With the reduced number of retained modes in each rotor, the overall accuracy of the drivetrain model was compromised.

We discussed how to effectively build both simplified linearized control models and very accurate nonlinear verification models. The accurate models could be used for multiple purposes as a virtual prototype of the industrial high-power high-speed drivetrain. This allowed, e.g., realistic testing scenarios that would otherwise require costly high-power equipment and a bunker. Other uses of the accurate model were diagnostics, monitoring, or application design iterations.

With the proposed coupling, the operation with external load was viable, and the controllability of the drivetrain could be achieved with minimum control tuning and without the need for hardware redesign. The rotor dynamic changes of the AMB–rotor, as seen by the controller, were limited to small frequency shifts without much change in the dominant bending mode shape. The control of rigid modes was not significantly affected. Similar methods could be generalized to other applications with long shafts or beams transmitting forces in cases where the application was not known precisely in advance. Further research topics related to the faults include, e.g., unbalance in different sections of the coupling and its significance for the dynamics and control adaptivity for different applications.

Acknowledgment

The authors would like to thank the engineering, technical, management, and steering teams behind the project.

References

[1] R. P. Jastrzebski et al., "Dynamics of high-power multi-rotor system," in *Proc. IEEE Int. Conf. Elect. Mach.*, 2022, pp. 1225–1231.

[2] Z. Liu, A. Chiba, Y. Irino, and Y. Nakazawa, "Optimum pole number combination of a buried permanent magnet bearingless motor and test results at an output of 60 kW with a speed of 37000 r/min," *IEEE Open J. Ind. Appl.*, vol. 1, pp. 33–41, 2020.

[3] Y. Gai et al., "Numerical and experimental calculation of CHTC in an oil-based shaft cooling system for a high-speed high-power PMSM," *IEEE Trans. Ind. Electron.*, vol. 67, no. 6, pp. 4371–4380, Jun. 2020.

[4] G. Du, W. Xu, J. Zhu, and N. Huang, "Power loss and thermal analysis for high-power high-speed permanent magnet machines," *IEEE Trans. Ind. Electron.*, vol. 67, no. 4, pp. 2722–2733, Apr. 2020.

[5] K. K. Nielsen, C. R. H. Bahl, N. A. Dagnaes, I. F. Santos, and R. Bjørk, "A passive permanent magnetic bearing with increased axial lift relative to radial stiffness," *IEEE Trans. Magn.*, vol. 57, no. 3, Mar. 2021, Art. no. 8300108.

[6] J. Van Verdeghem and B. Dehez, "Fully passively levitated self-bearing machine implemented within a reaction wheel," *IEEE Trans. Ind. Appl.*, vol. 57, no. 6, pp. 5782–5795, Nov./Dec. 2021.

[7] A. Filatov, L. Hawkins, and P. McMullen, "Passive radial bearing with active damper for downhole natural gas compressor," *IEEE Trans. Ind. Appl.*, vol. 57, no. 6, pp. 6801–6811, Nov./Dec. 2021.

[8] R. P. Jastrzebski, D. Kepsu, A. Putkonen, I. Martikainen, A. Zhuravlev, and S. Madanzadeh, "Competitive technology analysis of a double stage kinetic compressor for 0.5 MW heat pumps for industrial and residential heating," in *Proc. IEEE Int. Electric Mach. Drives Conf.*, 2021, pp. 1–7.

[9] R. P. Jastrzebski, A. Putkonen, E. Kurvinen, and O. Pyrhonen, "Design and modeling of 2 MW AMB rotor with three radial bearing-sensor planes," *IEEE Trans. Ind. Appl.*, vol. 57, no. 6, pp. 6892–6902, Nov./Dec. 2021.

[10] R.S. Srinivas, R. Tiwari, and C. Kannababu, "Model based analysis and identification of multiple fault parameters in coupled rotor systems with offset discs in the presence of angular misalignment and integrated with an active magnetic bearing," *J. Sound Vib.*, vol. 450, pp. 109–140, 2019.

[11] Y. Lei, B. Yang, X. Jiang, F. Jia, N. Li, and A. K. Nandi, "Applications of machine learning to machine fault diagnosis: A review and roadmap," *Mech. Syst. Signal Process.*, vol. 138, 2020, Art. no. 106587.

This article has been accepted for inclusion in a future issue of this journal. Content is final as presented, with the exception of pagination.

[12] Y. Xu, J. Zhou, Z. Lin, and C. Jin, "Identification of dynamic parameters of active magnetic bearings in a flexible rotor system considering residual unbalances," *Mechatronics*, vol. 49, pp. 46–55, 2018.
[13] D. Bobylev, T. Choudhury, J. O. Miettinen, R. Viitala, E. Kurvinen, and J. Sopanen, "Simulation-based transfer learning for support stiffness identification," *IEEE Access*, vol. 9, pp. 120652–120664, 2021.
[14] H. Gao, X. Meng, and K. Qian, "The impact analysis of beating vibration for active magnetic bearing," *IEEE Access*, vol. 7, pp. 134104–134112, 2019.
[15] S. Zheng, B. Han, R. Feng, and Y. Jiang, "Vibration suppression control for AMB-supported motor driveline system using synchronous rotating frame transformation," *IEEE Trans. Ind. Electron.*, vol. 62, no. 9, pp. 5700–5708, Sep. 2015.
[16] S. Zheng, H. Li, C. Peng, and Y. Wang, "Experimental investigations of resonance vibration control for noncollocated AMB flexible rotor systems," *IEEE Trans. Ind. Electron.*, vol. 64, no. 3, pp. 2226–2235, Mar. 2017.
[17] C.-S. Kim and C.-W. Lee, "In situ runout identification in active magnetic bearing system by extended influence coefficient method," *IEEE/ASME Trans. Mechatron.*, vol. 2, no. 1, pp. 51–57, Mar. 1997.
[18] S.-L. Chen, S.-Y. Lin, and C.-S. Toh, "Adaptive unbalance compensation for a three-pole active magnetic bearing system," *IEEE Trans. Ind. Electron.*, vol. 67, no. 3, pp. 2097–2106, Mar. 2020.
[19] P. Kumar and R. Tiwari, "Finite element modelling, analysis and identification using novel trial misalignment approach in an unbalanced and misaligned flexible rotor system levitated by active magnetic bearings," *Mech. Syst. Signal Process.*, vol. 152, pp. 107–454, 2021.
[20] P. Kumar and R. Tiwari, "Dynamic analysis and identification of unbalance and misalignment in a rigid rotor with two offset discs levitated by active magnetic bearings: A novel trial misalignment approach," *Propulsion Power Res.*, vol. 10, no. 1, pp. 58–82, 2021.
[21] A. Noshadi and A. Zolfagharian, "Unbalance and harmonic disturbance attenuation of a flexible shaft with active magnetic bearings," *Mech. Syst. Signal Process.*, vol. 129, pp. 614–628, 2019.
[22] A. D. Graham and M. Wimshurst, "The high speed oil free intelligent motor-compressor," in *Proc. 5th Eur. Conf. Power Electron. Appl.*, 1993, pp. 384–389.
[23] B. Dong, K. Wang, B. Han, and S. Zheng, "Thermal analysis and experimental validation of a 30 kW 60000 r/min high-speed permanent magnet motor with magnetic bearings," *IEEE Access*, vol. 7, pp. 92184–92192, 2019.
[24] D. Kepsu, E. Kurvinen, J. Tiainen, J. Honkatukia, T. Turunen-Saaresti, and R. P. Jastrzebski, "Interdisciplinary design of a high-speed drivetrain for a kinetic compressor in a high-temperature heat pump," *IEEE Access*, vol. 9, pp. 143877–143900, 2021.
[25] E. Kurvinen et al., "Design and manufacturing of a modular low-voltage multimegawatt high-speed solid-rotor induction motor," *IEEE Trans. Ind. Appl.*, vol. 57, no. 6, pp. 6903–6912, Nov./Dec. 2021.
[26] C. Chamroon, M. O. T. Cole, and T. Wongratanaphisan, "An active vibration control strategy to prevent nonlinearly coupled rotor-stator whirl responses in multimode rotor-dynamic systems," *IEEE Trans. Control Syst. Technol.*, vol. 22, no. 3, pp. 1122–1129, May 2014.
[27] H. A. DeSmidt, K. W. Wang, and E. C. Smith, "Multi-harmonic adaptive vibration control of AMB-Driveline systems with non-constant velocity flexible couplings," *Int. Des. Eng. Tech. Conf. Comput. Inf. Eng. Conf.*, 2008, pp. 1995–2005.
[28] Q. Chen, G. Liu, and B. Han, "Suppression of imbalance vibration in AMB-rotor systems using adaptive frequency estimator," *IEEE Trans. Ind. Electron.*, vol. 62, no. 12, pp. 7696–7705, Dec. 2015.
[29] H. Nelson, "A finite rotating shaft element using Timoshenko beam theory," *J. Mech. Des.*, vol. 102, no. 4, pp. 793–803, 1980.
[30] W. Chen and E. Gunter, *Introduction to Dynamics of Rotor-Bearing Systems*. Victoria, Canada: Trafford Publishing, 2005.
[31] J. Narsakka, "Coupling design and analysis for high-speed drivetrain supported by three active magnetic bearings," M.S. thesis, LUT School of Energy System, LUT University, Lappeenranta, Finland, 2022.
[32] A. Zhuravlev, R. P. Jastrzebski, and L. Chechurin, "Numerical study of robust control for an AMB rotor with uncertain speed," in *Proc. IEEE/ASME Int. Conf. Adv. Intell. Mechatronics*, 2022, pp. 1799–1806.
[33] "Mechanical vibration — Vibration of rotating machinery equipped with active magnetic bearings—Part 3: Evaluation of stability margin," Standard ISO 14839-3:2006, International Standard Organisation, Geneva, Switzerland, 2006.

Rafal P. Jastrzebski (Senior Member, IEEE) received the M.Sc. degree in microelectronics from the Technical University of Lodz, Lodz, Poland, in 2002, and the D.Sc. degree in electrical engineering from the Lappeenranta University of Technology (LUT), Lappeenranta, Finland, in 2007.

From 2009 to 2011, he was a Postdoctoral Researcher with the Academy of Finland, Helsinki, Finland. From 2013 to 2018, he was an Academy Research Fellow. He is currently an Associate Professor (tenured) with the University of Turku, Turku, Finland, and Docent with LUT University. His research interests include mechatronic systems, digital control, energy applications, active magnetic bearings, magnetic levitation systems, and bearingless machines.

Atte Putkonen received the M.Sc. (Tech.) degree in electrical engineering in 2020 from Lappeenranta–Lahti University of Technology (LUT), Lappeenranta, Finland, where he is currently a doctoral student with the LUT School of Energy Systems.

His research interests include identification and control of bearingless machines and active magnetic bearing systems.

Andrei Zhuravlev received the master's degree in a double degree program between the Lappeenranta–Lahti University of Technology, Lappeenranta, Finland (LUT) and Saint Petersburg Electrotechnical University, Saint Petersburg, Russia. He completed the exchange studies with the Zhejiang Ocean University, Zhoushan, China. He is currently a doctoral student with the LUT School of Energy Systems, LUT.

His research interests include control of active magnetic bearings and bearingless machines.

Tuhin Choudhury was born in 1989. He received the B.Sc. (Tech.) degree in mechanical engineering from the Sikkim Manipal University, Gangtok, India, in 2011, and the M.Sc. (Tech.) and D.Sc. (Tech.) degrees in mechanical engineering from the Lappeenranta University of Technology, Lappeenranta, Finland, in 2018 and 2022, respectively.

From 2011 to 2016, he was a design engineer on the development of medical devices and diagnostic instruments. His research interests include designing, modeling, and simulation of rotating machines, and the analysis of rotor behavior to understand the root cause of unwanted vibrations, specifically due to unbalance.

This article has been accepted for inclusion in a future issue of this journal. Content is final as presented, with the exception of pagination.

Eerik Sikanen received the M.Sc. degree in mechanical engineering and the D.Sc. (Tech.) degree in mechanical engineering from the Lappeenranta University of Technology, Lappeenranta, Finland, in 2014 and 2018, respectively.

His research interests include high-speed rotor dynamics analysis, general vibration dynamics of rotating machinery, and 3-D solid finite element modeling of high-speed machinery and systems including contact and thermomechanical effects.

Emil Kurvinen was born in 1988. He received the M.Sc. (Tech.) and D.Sc. (Tech.) degrees in mechanical engineering from the Lappeenranta University of Technology, Lappeenranta, Finland, in 2012 and 2016, respectively. He is currently a machine design Professor with the University of Oulu, Oulu, Finland. He has a solid background in machine design, especially in the design, simulation, and analysis of rotating machines. His research interests include rotating machines, especially high-speed machines, digital twins, and the integration of industrial engineering and management into technology.

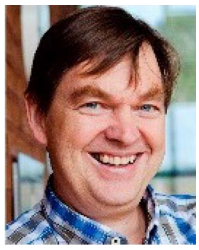

Juha J. Pyrhönen (Senior Member, IEEE) born in 1957 in Kuusankoski, Finland. He received the D.Sc. degree in electrical engineering from the Lappeenranta University of Technology (LUT), Lappeenranta, Finland, in 1991.

He became a Professor of electrical machines and drives in 1997 with LUT. He is engaged in research and development of electric motors and power-electronic-controlled drives. He has wide experience in the research and development of special electric drives for, e.g., distributed power production, traction, and high-speed applications. Permanent magnet materials and applying them in machines play an important role in his research. Currently, he is also studying opportunities of using carbon-based materials in electrical machines.